

A Novel Coded Excitation Scheme to Improve Spatial and Contrast Resolution of Quantitative Ultrasound Imaging

Jose R. Sanchez, *Student Member, IEEE*, Darren Pocci, *Student Member, IEEE*, and Michael L. Oelze, *Senior Member, IEEE*

Abstract—Quantitative ultrasound (QUS) imaging techniques based on ultrasonic backscatter have been used successfully to diagnose and monitor disease. A method for improving the contrast and axial resolution of QUS parametric images by using the resolution enhancement compression (REC) technique is proposed. Resolution enhancement compression is a coded excitation and pulse compression technique that enhances the -6 -dB bandwidth of an ultrasonic imaging system. The objective of this study was to combine REC with QUS (REC-QUS) and evaluate and compare improvements in scatterer diameter estimates obtained using the REC technique to conventional pulsing methods. Simulations and experimental measurements were conducted with a single-element transducer ($f/4$) having a center frequency of 10 MHz and a -6 -dB bandwidth of 80%. Using REC, the -6 -dB bandwidth was enhanced to 155%. Images for both simulation and experimental measurements contained a signal-to-noise ratio of 28 dB. In simulations, to monitor the improvements in contrast a software phantom with a cylindrical lesion was evaluated. In experimental measurements, tissue-mimicking phantoms that contained glass spheres with different scatterer diameters were evaluated. Estimates of average scatterer diameter in the simulations and experiments were obtained by comparing the normalized backscattered power spectra to theory over the -6 -dB bandwidth for both conventional pulsing and REC. Improvements in REC-QUS over conventional QUS were quantified through estimate bias and standard deviation, contrast-to-noise ratio, and histogram analysis of QUS parametric images. Overall, a 51% increase in contrast and a 60% decrease in the standard deviation of average scatterer diameter estimates were obtained during simulations, while a reduction of 34% to 71% was obtained in the standard deviation of average scatterer diameter for the experimental results.

I. INTRODUCTION

IN ultrasound, a 2-D brightness image, known as a B-mode image, yields qualitative information from a cross section of the tissue being interrogated. These B-mode images are generated by digitally sampling radio-frequency signals backscattered from tissue that are then converted into a gray-scale image by detecting the envelope. This process removes the frequency-dependent information

contained in the backscattered radio frequency signal. However, quantitative information about the underlying tissue microstructure, structures that are smaller than the ultrasound wavelength, can be extracted from the frequency dependence of the backscattered radio frequency signals [1].

Quantitative ultrasound (QUS) imaging techniques based on ultrasonic backscatter have been used to characterize tissue and to diagnose and monitor disease successfully. The theoretical foundation for tissue characterization using spectral analysis was laid out by Lizzi *et al.* [1]. Applications where the frequency-dependent backscatter information was used to quantify tissues include ocular tumors [2]–[9], liver and kidney tissue characterization [9]–[13], prostate tumors [14], [15], breast tumors [16]–[22], and vascular abnormalities [23], [24]. These applications have established the potential importance of QUS in the ultrasonics community.

To model the scattering process for tissue characterization, it is assumed that tissues conduct sound as an inhomogeneous fluid [25]. Furthermore, the model assumes scatterers of finite sizes that can be approximated by simple geometric shapes and therefore characterized by a size and concentration [20]. In addition, the size and shape of the scatterers determine the magnitude at which a specific frequency of sound will be scattered [20]. Therefore, with QUS, the normalized backscattered power spectrum from a region of interest (ROI) can be parameterized and related to tissue microstructure [20]. For example, the average scatterer diameter and average acoustic concentration of underlying scatterers can be estimated from the normalized backscattered power spectrum [20]. Parametric images can be constructed by associating the estimated scatterer properties with ROIs at different spatial locations. These ROIs correspond to pixels in the parametric image whose color or intensity corresponds to a particular parameter value. The size of the ROI corresponds to the spatial resolution of the parametric image and is dictated by the number of independent scan lines in the lateral extent and axially by the spatial distance delineated by a range gating function. By decreasing the size of the ROI, the spatial resolution of the parametric image is improved. Unfortunately, a trade-off exists between the accuracy and precision of the scatterer property estimates and the size of the ROI [26]. Furthermore, one of the most important factors reducing the effectiveness of QUS imaging techniques is the low contrast resolution between diseased tis-

Manuscript received July 25, 2008; accepted June 20, 2009. This work was supported by a grant from the National Institutes of Health (R21 EB006741).

J. R. Sanchez is with the Department of Electrical and Computer Engineering, Bradley University, Peoria, IL (e-mail: jsm@bradley.edu).

D. Pocci and M. L. Oelze are with the Department of Electrical and Computer Engineering, University of Illinois at Urbana-Champaign, Urbana, IL.

Digital Object Identifier 10.1109/TUFFC.2009.1294

sues and normal tissues or between benign and malignant tumors. The contrast resolution of QUS images depends on the variance of QUS estimates. The variance of QUS estimates decreases with increasing bandwidth of the imaging system [20]. Therefore, an imaging system with larger bandwidth would yield lower variance in spectral estimates.

The usefulness of parametric imaging for characterization and diagnosis of diseased tissue has improved due to the advancement of signal processing techniques that improve the accuracy of the estimates from backscatter. Recently, Kanzler and Oelze [27] improved QUS estimates of average scatterer diameter in tissue-mimicking phantoms by using coded excitation and pulse compression. In this study, the increase in echo signal-to-noise ratio (eSNR) achieved through coded excitation resulted in increased depths (50%) at which accurate average scatterer diameter estimates could be obtained versus conventional pulsing (CP) techniques. Finally, in this work, the coded excitation and pulse compression scheme had a minimal effect on the estimate variance because it reduced the estimate variance at most depths by a few percent.

In the current study, a coded excitation and pulse compression technique, known as resolution enhancement compression (REC) [28], will be used to improve the bias and standard deviation of average scatterer diameter estimates. The REC technique can increase the bandwidth of the ultrasonic imaging system by a factor of 2 without the presence of large side lobes often observed with coding and pulse compression techniques. In addition to the bandwidth enhancement, the REC technique has the typical coded excitation benefits, such as deeper penetration, which is due to increases in the eSNR. Furthermore, a larger eSNR translates into a larger usable bandwidth of the imaging system. Usable bandwidth in this work is defined as the segment of the backscattered power spectrum that is 6 dB above the noise floor. Chaturvedi and Insana [29] observed that the standard deviation in scatterer property estimates was inversely proportional to the bandwidth of the imaging system. Therefore, the goal of this study was to combine the REC technique with QUS, which will be described as REC-QUS, and evaluate the improvements in standard deviation of average scatterer diameter estimates due to the enhanced bandwidth and gain in eSNR. Another goal was to extend the trade-off of estimate standard deviation and the spatial resolution of the parametric image (ROI size). Both a broadening of the bandwidth and gain in eSNR should yield improved QUS estimates, which in turn will improve the diagnostic capabilities of QUS imaging techniques for clinical applications.

II. METHODS AND PROCEDURES

A. REC

REC is a coded excitation and pulse compression technique that uses convolution equivalence (shown in Fig.

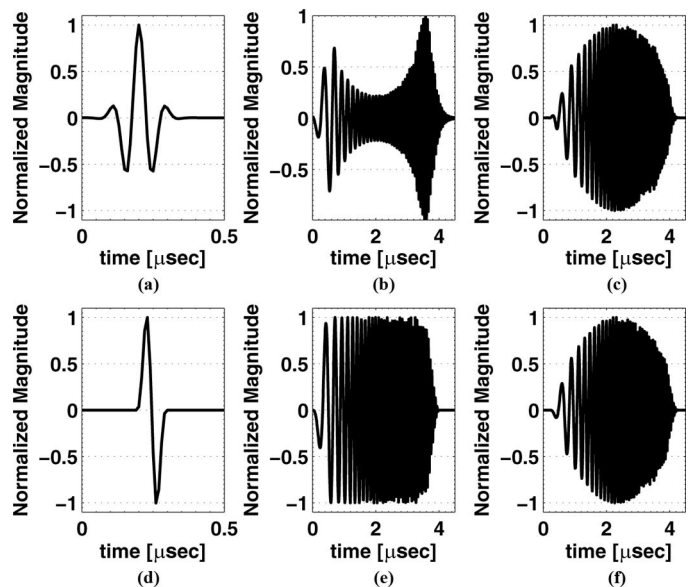


Fig. 1. Convolution equivalence scheme from a Matlab simulation: (a) pulse-echo impulse response for a source with an 80% -6 -dB bandwidth, (b) pre-enhanced chirp used to excite the 80% bandwidth source, (c) convolution of 80% source with pre-enhanced chirp, (d) pulse-echo impulse response of a desired source with a 150% -6 -dB bandwidth, (e) linear chirp used to excite the 150% bandwidth source, and (f) convolution of 150% source with linear chirp.

1) to improve the axial resolution and enhance the bandwidth of an ultrasonic imaging system. In REC, a desired impulse response, $h_2(t)$ is synthetically generated so that time duration is less when compared with the ultrasonic system pulse-echo impulse response, $h_1(t)$ as shown in Figs. 1(a) and (d). As a result, the corresponding bandwidth of $h_2(t)$ is larger than the bandwidth of $h_1(t)$. To obtain the desired impulse response for the imaging system, a pre-enhanced chirp is used to excite the source. The pre-enhanced chirp is used to excite an ultrasonic source selectively with different energies at chosen frequencies. By exciting the transducer with the pre-enhanced chirp, the bandwidth is enhanced due to the increase of energy in the frequency bands that normally would be filtered in some measure by the bandpass nature of the transducer. Conceptually, to obtain a constant eSNR per frequency channel across the desired bandwidth, the additional amount of energy required on transmit at the outer frequency bands will depend on the original transducer's bandwidth and the amount of bandwidth boost desired.

Once the source is excited with a pre-enhanced chirp, the received echo is compressed using a Wiener filter based on convolution equivalence. The resulting backscattered signal has an impulse response $h_2(t)$. Wiener filtering is described by the following equation:

$$\beta_{\text{REC}}(f) = \frac{V_{\text{lin}}^*(f)}{|V_{\text{lin}}'(f)|^2 + \gamma e^{\text{SNR}^{-1}}(f)}, \quad (1)$$

where f is frequency, and γ is a smoothing parameter that controls the trade-offs among bandwidth enhancement

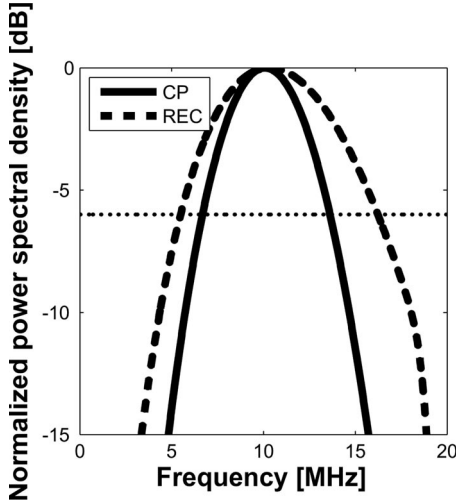


Fig. 2. Simulated power spectrum of conventional pulsing (CP) and resolution enhancement compression (REC) (compressed) from a point scatterer in an attenuated medium with $\alpha = 0.5 \text{ dB MHz}^{-1}\text{cm}^{-1}$ using a 10-MHz source.

(axial resolution), gain in eSNR, and sidelobe levels. $V'_{\text{lin}}(f)$ is the Fourier spectrum of a modified linear chirp that is used to restore convolution equivalence as the signal is slightly altered and filtered by electronics. $V'_{\text{lin}}(f)$ is defined as

$$V'_{\text{lin}}(f) = \frac{H_2^*(f)}{|H_2(f)|^2 + |\eta(f)|^2} \cdot H_{\text{out}}(f), \quad (2)$$

where $H_2(f)$ is the Fourier spectrum of the desired response, $h_2(t)$, and $H_{\text{out}}(f)$ is the Fourier spectrum of an echo obtained from a planar reflector located at the focus upon excitation with a preenhanced chirp. $\text{eSNR}(f)$ is the average eSNR [30] per frequency channel and is defined as

$$\overline{\text{eSNR}}(f) = \frac{|H_{2c}(f)|^2 E\{|F(f)|^2\}_f}{E\{|\eta(f)|^2\}_\eta}, \quad (3)$$

where $|F(f)|^2$ is the power spectral density (PSD) of the object function, $|\eta(f)|^2$ is the PSD of the noise, and $|H_{2c}(f)|^2$ is the PSD of the echo signal over noise, $h_{2c}(t)$, which is defined as

$$h_{2c}(t) = E\{g(t)\}_{\text{noise}}, \quad (4)$$

where E is the expectation value of the argument and $g(t)$ is the echo signal over noise. To obtain eSNR experimentally, a measure of the noise per frequency channel is first obtained by estimating the mean of the PSD of a noise measurement from a water bath that contains no imaging target while using the same equipment settings. Thereafter, the signal (which contains noise) power is divided by the noise per frequency channel to get eSNR.

Fig. 2 illustrates the enhanced bandwidth of REC by displaying the PSD of the CP and REC waveforms due

to a reflection from a point scatterer in a simulated attenuating medium, with $\alpha = 0.5 \text{ dB MHz}^{-1}\text{cm}^{-1}$ using a 10-MHz source and an axial distance of 50 mm. The bandwidth at -6 dB was 7.2 MHz and 12.1 MHz for CP and REC, respectively. Original source bandwidth at -6 dB before the inclusion of attenuation and scattering effects into the simulation was 7.9 MHz and 15.5 MHz for CP and REC, respectively.

B. QUS

Average scatterer diameter can be estimated from the frequency dependence of the normalized backscattered power spectrum. To estimate the average scatterer diameter from the normalized backscattered power spectrum, the following assumptions were made: multiple scattering is negligible, the scatterers are uniformly and randomly located spatially, and the distribution of scatterer sizes is small relative to the mean size. In soft tissues, the frequency dependence of the normalized backscattered power spectrum has been modeled by the acoustic intensity form factor, F , which is related to a 3-D spatial autocorrelation function that describes the material properties of the scatterers [1], [31]. For soft tissues, the theoretical power spectrum [31] is formulated by

$$P_{\text{theor}}(f) = B(L, q)C(a_{\text{eff}}, n_z)f^4 F(f, a_{\text{eff}}) \quad (5)$$

where f is the frequency, B is a constant that depends on L , which is the axial length of the range gate, and q , which is the ratio of the source radius to distance from the ROI. C is a constant depending on the average effective radius a_{eff} of the scatterers and n_z is the average acoustic concentration.

The normalized power spectrum is calculated through [32]

$$P_{\text{norm}}(f) = \frac{A(f, L)}{N} \left(\frac{R}{2}\right)^2 \sum_{n=1}^N \frac{P_m(f)}{P_{\text{ref}}}, \quad (6)$$

where A is an attenuation compensation function, N is the number of gated scan lines in the ROI to be averaged, P_{ref} is a reference power spectrum, R is the reflectivity of a planar surface used to obtain the reference power spectrum, and $P_m(f)$ is the power spectrum calculated from a range gated signal. The reference power spectrum, P_{ref} , was obtained by measuring the output of the transducer when a plexiglass surface was positioned at the focus of the source [1].

1) *Attenuation Compensation*: Frequency-dependent attenuation alters the shape of the power spectrum as attenuation increases with frequency. Hence, if the attenuation is not compensated for, the average scatterer diameter will be overestimated. In simulations and experimental measurements, to compensate for attenuation, a point compensation scheme was used. Point compensation [31] is described by

$$A_{\text{pc}}(f, x) = e^{4\alpha(f)R_1}, \quad (7)$$

where $\alpha(f)$ is the frequency-dependent attenuation and R_1 is the distance between the front end of the object and the front end of the gated region.

2) *Bandwidth*: As previously stated, QUS techniques that make use of spectral information would be greatly improved by larger bandwidth imaging systems. Larger bandwidth leads to smaller variance in spectral estimates in QUS. Smaller variance in spectral estimates means that tissues will be more differentiable with QUS imaging techniques. The variance of average scatterer diameter estimates when assuming a Gaussian form factor is inversely proportional to the bandwidth squared of the imaging system and is described by the following equation [20], [29]:

$$\text{var } \widehat{D} = \frac{2.09 \times 10^{-2}}{D^2} \left[\sum_{j=1}^M f_j^4 - M \cdot E\{f^2\}^2 \right]^{-1}, \quad (8)$$

where \widehat{D} is the estimated average scatterer diameter, D is the actual average scatterer diameter in the ROI, f is frequency, f_j are frequency points in the analysis bandwidth that are uncorrelated, and M is the total number of data points used in the analysis bandwidth. Furthermore, (8) indicates that the variance in scatterer property estimates is inversely proportional to the average scatterer diameter squared. Note that although the expression in (8) is only true for monodisperse scattering ensembles, the bandwidth-variance relationship still holds for a distribution of scatterer sizes.

C. Simulations

Computer simulations were carried out in Matlab (MathWorks, Natick, MA) to characterize the performance of the REC-QUS technique. The simulations used a received pulse-echo pressure field model [33] described as

$$g[x, y, t] = h_1(t) * f(x, y) * h_{\text{pe}}(y, t), \quad (9)$$

where x represents the axial spatial coordinate, y represents the lateral spatial coordinate, $f(x, y)$ is the scattering function, and $h_{\text{pe}}(y, t)$ is the modified pulse-echo spatial impulse response that takes into consideration the geometry of the transducer to the spatial extent of the scattered field (beam diffraction).

The pulse-echo impulse response, $h_1(nT, x)$, for CP was approximated by

$$h_1(t) = e^{-(t^2 - \tau)/\sigma_t^2} \cos(\omega t), \quad (10)$$

where σ_t^2 is the second central moment of the Gaussian pulse, which dictates the bandwidth of the pulse. A shift, τ , was added to $h_1(t)$, to make the pulse causal. The generated pulse-echo impulse response was located at the focus

of a 10-MHz single-element transducer ($f/4$) with a -6 -dB fractional bandwidth of 80%.

For the REC, the impulse response function, $h_2(t)$, was constructed to have a -6 -dB fractional bandwidth of 150% by gating a sinusoid of 4 cycles with a Hanning window

$$w(n) = \begin{cases} 0.5 \left(1 - \cos\left(\frac{2\pi n}{L_H - 1}\right) \right), & 0 \leq n \leq L_H - 1 \\ 0, & \text{otherwise} \end{cases} \quad (11)$$

where n is an integer and L_H is the number of samples in the window. A Hanning window of a length of $L_H = 24$ was used.

The spatial response for a circular focused piston source was simulated as a circular Gaussian beam, which is defined as

$$h_{\text{pe}}(y, t) = \delta\left(t - \frac{2R_d}{c}\right) e^{-y^2/\sigma_y^2}, \quad (12)$$

where R_d is the distance from the source to target in space, c is the speed of sound of the medium, which was set to 1540 m/s, and σ_y is the -6 -dB lateral beamwidth, which is equal to 0.62 mm.

Ten simulations were performed for each of the 2 types of phantoms used. Descriptions of the 2 simulated phantoms are shown in Table I. Phantom S1 and S2 contain an average of 15 point scatterers per resolution cell volume. These scatterers have an f^4 dependence on the backscatter power spectrum. However, to model soft tissue scattering and to obtain average scatterer diameter estimates, the simulated phantoms were modified by the spherical Gaussian form factor [31]. The spherical Gaussian form factor was used to model soft tissue scattering, which is described by

$$F_{\text{Gauss}}(f) = e^{-12.159f^2 a_{\text{eff}}^2}. \quad (13)$$

The spherical Gaussian form factor has been used by various researchers to model the scattering of soft tissues [4], [20], [31], [34]–[36]. In addition, the backscattered data was reduced by the frequency-dependent attenuation corresponding to the distance of the scatterer from the source. The attenuation was set to 0.5 dB MHz⁻¹ cm⁻¹. Phantom S1 was used to evaluate the effects that REC had on the spatial resolution of QUS images due to the increase in bandwidth. Phantom S2 consisted of the same parameters of phantom S1 except that it contained a cylindrical lesion of 6 mm in radius that was centered in a background region. Phantom S2 was used to evaluate the effects that REC had on the contrast resolution of QUS images due to the improvements in standard deviation of average scatterer diameter estimates. Both phantoms S1 and S2 were placed 40 mm from the simulated source, which had a focal depth of 50 mm.

The backscatter coefficient estimates [32] were obtained by

$$\sigma_b(f) = \frac{3.87(R_0 + R_1)^2}{A_o L} P_{\text{norm}}(f), \quad (14)$$

TABLE I. SIMULATED PHANTOM PROPERTIES.

Property ¹	Phantom		
	S1	S2	
		Lesion	Background
Phantom dimensions:			
length, width, height (mm)	20 × 30 × 1.2	20 × 30 × 1.2	
Scatterer type	Gaussian	Gaussian	Gaussian
Scatterer diameter (μm)	50	60	50
Lesion diameter (mm)	—	12	—
Nominal sound speed (m/s)	1540	1540	1540
Nominal attenuation (dB/(MHz cm))	0.5	0.5	0.5
CP: ka (10 MHz @ -6 dB)	0.68–1.41	0.81–1.69	0.68–1.41
REC: ka (10 MHz @ -6 dB)	0.54–1.71	0.65–2.05	0.54–1.71

¹Conventional pulsing; REC = resolution enhancement compression.

where A_o is the surface area of the transducer, R_0 is the on-axis distance between the transducer and the front end of the object being imaged, and R_1 is the distance between the front end of the object and the front end of the gated region.

The received radio frequency backscatter data were sampled at a rate of 100 MHz and the transducer was translated laterally in increments of 0.31 mm (50% overlap). For phantom S2, the size of the ROIs was selected by using the optimal axial and lateral resolution for estimating scatterer properties [26]. Axially, individual scan lines were gated with a rectangular window of a length that would correspond to 5.5 CP axial pulse lengths. Laterally, a distance of 5 lateral beamwidths was used, which corresponds to 10 scan lines because data was acquired with a 50% beamwidth overlap between scan lines. Therefore, each ROI was a rectangle 1.52 mm × 4.15 mm. However, ROIs were overlapped both laterally and axially by 66%; therefore, the effective ROI size after averaging was 0.50 mm × 1.25 mm. For phantom S1, the size of the ROI was varied in the axial extent because the goal of this study was to evaluate the estimate bias and standard deviation as a function of gate length.

Estimates of average scatterer diameter were obtained by approximating the measured power spectrum by a best-fit line technique [20]. Specifically, with this technique estimates were obtained by comparing the logarithm of the measured backscattered power spectrum (6) with the logarithm of the theoretical power spectrum (5) and then subtracting $10\log_{10}f^4$ from both sides, which yields

$$10\log_{10}P_{\text{norm}}(f) - 10\log_{10}f^4 \approx m(a_{\text{eff}})f^2 + b(n_z, a_{\text{eff}}, L, q). \quad (15)$$

Eq. (15) describes a straight line, $y = mx + b$, where $x = f^2$, m is the slope and is a function of a_{eff} , and b is the intercept and is a function of a_{eff} , n_z , q , and L . Finally, estimates were obtained by using least-squares analysis to find the best-fit slope on the measured and processed data from (15) using an analysis bandwidth corresponding to the -6-dB bandwidth of the simulated source.

D. Experiments

Measurements were performed to validate the improvements afforded by the REC-QUS technique in an experimental setting. A single-element weakly focused ($f/4$) transducer with a center frequency of 10 MHz was used to image phantoms by translating the transducer laterally. The transducer had a -6-dB pulse-echo bandwidth of 80% along with a -6-dB pulse-echo beamwidth of 0.67 mm. These parameters were measured using the wire technique [37] for transducer characterization. Using REC, the -6-dB pulse-echo bandwidth was enhanced to 155%. There were 2 different experimental setups used; one for CP and another one for REC experiments. These setups would contain different noise levels due to the use of different excitation systems; therefore, to avoid errors in the comparisons, the noise levels were normalized so that they contained the same eSNR. Normalization of eSNR was accomplished by adding zero-mean white Gaussian noise to the CP radio frequency echo waveforms because REC had the lower eSNR before compression. The 2 experimental setups are described by Fig. 3.

Measurements from 4 physical phantoms were obtained to evaluate the performance of REC-QUS versus conventional QUS methods. Descriptions of the 4 physical phantoms used in the experiments are shown in Table II. The phantoms were cylindrical samples bounded within an acrylic housing that contained a 25-μm Saran-Wrap plastic film (Dow Chemical, Midland, MI) [38] on the parallel flat surfaces. The Saran-Wrap layer served as a window for transmission of the ultrasound waves between water and the tissue-mimicking phantom. Therefore, to obtain correct estimates of phantom parameters the frequency-dependent transmission coefficients of the Saran-Wrap layers need to be compensated. The transmission coefficient for a single layer of Saran-Wrap is given by [38]:

$$T(k) = \frac{2Z_f}{(Z_i + Z_f) \cos(k_{\text{saran}}l) + j\left(Z_{\text{saran}} + \frac{Z_i Z_f}{Z_{\text{saran}}}\right) \sin(k_{\text{saran}}l)}, \quad (16)$$

TABLE II. EXPERIMENTAL PHANTOM PROPERTIES.

Property ¹	Phantom			
	A	B	C	D
Scatterer	Glass spheres	Glass spheres	Glass spheres	Glass spheres
Materials	Agarose/n-propanol/ milk/H ₂ O	Agarose/n-propanol/ milk/H ₂ O	Agarose/n-propanol/ graphite/H ₂ O	Agarose/n-propanol/ graphite/H ₂ O
Scatterer diameter (μm)	75–90	9–43	45–53	45–53
Nominal sound speed (m/s)	1540	1540	1540	1540
Attenuation (dB/(MHz cm))	0.5	0.7	0.5	0.7
CP: ka (10 MHz @ -6 dB)	1.70–4.37	0.20–2.19	1.02–2.58	1.02–2.58
REC: ka (10 MHz @ -6 dB)	0.97–6.04	0.12–3.02	0.58–3.56	0.58–3.56

¹CP = conventional pulsing; REC = resolution enhancement compression.

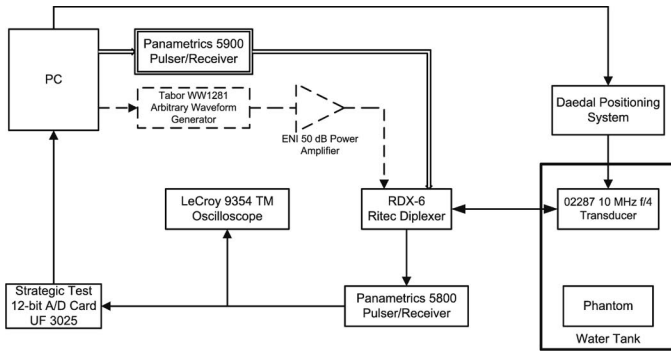


Fig. 3. Experimental setup used for CP and REC. Note that solid lines indicate components used in both CP and REC experiments, whereas double lines indicate a path only taken during CP experiments, and dashed lines indicate a path only taken during REC experiments.

where Z_i is the acoustic impedance of the incident material ($Z_i = 1.49$ MRayls), Z_f is the acoustic impedance of the final material ($Z_f = 1.49$ MRayls), and Z_{saran} is the acoustic impedance of the Saran-Wrap layer of length l ; k_{saran} is the wave number in the layer and is described by

$$k_{\text{saran}} = \frac{2\pi f}{c_{\text{saran}}} - j\alpha(f), \quad (17)$$

where c_{saran} is the speed of sound and α the frequency-dependent attenuation coefficient of the Saran-Wrap layer. More information about phantoms A and B can be found in [38]; likewise, more information about phantoms C and D can be found in [39].

The received radio frequency backscatter data were sampled at a rate of 100 MHz, and the transducer was translated laterally in increments of 0.33 mm (50% overlap). The size of the ROIs was selected by using the optimal axial and lateral resolution for estimating scatterer properties [26]. Axially, individual scan lines were gated with a rectangular window of a length that would correspond to 15 CP axial pulse lengths. Laterally, 5 lateral beamwidths were used, which corresponds to 10 scan lines because data were acquired with a 50% beamwidth overlap between scan lines. Therefore, each ROI was a rectangle 3.3 mm \times 3 mm. However, ROIs were overlapped both laterally and axially by 66%; therefore, the effective ROI size after averaging was 1.1 mm \times 1 mm.

Estimates of average scatterer diameter were obtained by minimizing the average squared deviation (MASD) as a function of average scatterer diameter,

$$\hat{D} = \min_{\text{ASD}} (E\{(X(f, \text{ASD}) - E\{X(f, \text{ASD})\})^2\}), \quad (18)$$

where $X(f, \text{ASD})$ is $10\log_{10}(\sigma_b/\sigma_0)$ where σ_0 is the theoretical backscatter coefficient obtained from Faran's theory [40], [41] and σ_b is the backscatter coefficient from the phantom, which was estimated by using a broadband substitution method for weakly focused transducers [32]. Estimates of the backscatter coefficient were obtained using (14). The mean of $X(f, \text{ASD})$ is subtracted from $X(f, \text{ASD})$ such that the backscatter coefficient is calculated based on the shape, or frequency dependence, and independent of the magnitude of σ_b .

During experiments, large echoes due to the front surface of the phantoms were clipped because the A/D card had a voltage limitation of ± 0.5 V. This was an engineering trade-off, because gain was applied so that the backscatter behind the front surface fully spanned the dynamic range of the A/D card. However, a consequence of clipping AM and FM modulated signals is that, after compression, large sidelobes are introduced. As a result, the portion of the signal that was being clipped was replaced with zero-mean white Gaussian noise that contained the same variance introduced by the system [27].

In measurements, the phantoms were placed in a tank of 20°C degassed water such that the front of the phantoms was perpendicular to the beam axis of the transducer as shown in Fig. 4. Measurements of backscatter for all phantoms were obtained for 3 distances of R_1 : 10 mm, 15 mm, and 20 mm. Each distance represents a shift in the placement of the focus within the phantom. R_0 was decreased by the same amount R_1 was increased to maintain the sum of R_0 and R_1 constant. QUS parametric images for experimental measurements were generated by compounding the estimates for all 3 distances listed above. Reference pulses were obtained by reflecting an incident pulse off a plexiglass surface for both CP and REC. Because estimates require normalization with a reference spectrum that is located at the center of the gate, reference pulses were obtained in increments of 500 μm that spanned the entire depth of focus.

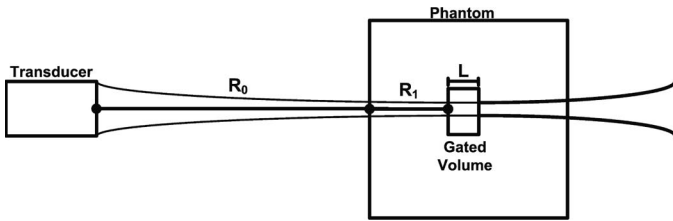


Fig. 4. Distance relationship between the transducer and phantoms used to obtain measurements. R_0 is the distance from transducer surface to phantom surface, while R_1 is the distance from phantom surface to the start of the gated region of length L . The focal depth is at $R_0 + R_1$.

E. Quality Metrics

To assess the REC-QUS technique, numerical simulations were implemented, and experimental measurements were acquired. The simulations and experiments used REC to increase the -6 -dB bandwidth of the imaging system for QUS and results were compared with CP methods. Therefore, to evaluate the performance of the REC-QUS technique against CP the following quality metrics were used:

1. Standard deviation: Estimate standard deviation is the estimation precision and is arguably the most important metric of QUS imaging. The main limitation of QUS imaging techniques when differentiating and characterizing tissues is the overlapping of estimate values due to the size of estimate standard deviation. By reducing estimate standard deviation, QUS imaging techniques will be more sensitive to tissue differences and improve diagnostic capability.
2. Bias: Estimate bias is the deviation of the simulated or measured QUS parameter from a reference scatterer diameter. The accuracy of the underlying structure is quantified by the bias of the scatterer property estimates. However, when evaluating the experimental measurements of physical phantoms, estimate mean will be used over estimate bias because the phantoms contain scatterers with varying diameters. In these cases, the out of range, i.e., the percentage of size estimates that are not bounded between the maximum and minimum average scatterer diameter, will be tallied to obtain a measure of correctness of estimation (estimates that do not deviate from the range).
3. Contrast-to-noise ratio (CNR): CNR is a quantitative measure that will assess image quality and describe the ability to perceive a lesion from the background region or lesion-free region. CNR [42] is defined as

$$\text{CNR} = \left| \frac{\mu_B - \mu_L}{\sqrt{\sigma_B^2 + \sigma_L^2}} \right|, \quad (19)$$

where μ_B and μ_L are the mean brightness of the background and the target lesion and σ_B^2 and σ_L^2 are the variance of the background and target, respec-

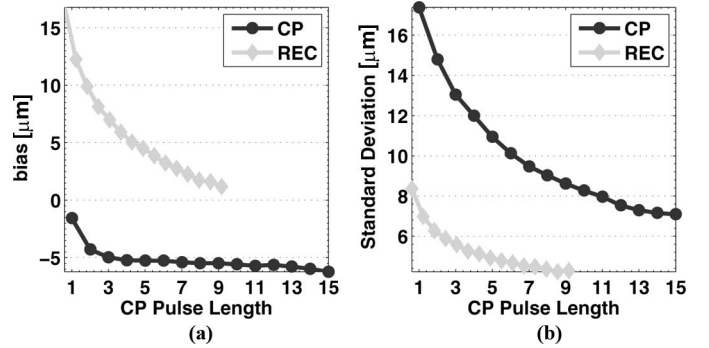


Fig. 5. (a) Bias and (b) standard deviation of average scatterer diameter estimates as a function of pulse length for 10 simulations of Phantom S1. Each tick mark on the abscissa is normalized to a conventional pulsing (CP) pulse length of one, which corresponds to 0.277 mm. Therefore, one resolution enhancement compression (REC) pulse length, which is 0.169 mm, would correspond to 0.610 CP pulse length.

tively. To avoid possible errors in the calculations due to attenuation, the evaluated ROIs in the background and the target lesion were of the same size and located at the same depth. CNR is a unitless quantity.

4. Histogram overlap: Histogram overlap is the percentage of pixels in the background and target lesion histograms that share the same pixel intensity. Histograms were made for same-sized regions for the target lesion and the background adjacent to the target. Like CNR, the histogram overlap is a measure of the detectability of the lesion from the background. Note that the number of points in the histograms will vary based on the size of the ROIs.

III. RESULTS

A. Simulations

Simulations of phantom S1 consisted of obtaining estimates by varying the size of the axial gate. The axial gate lengths evaluated for CP and REC were dictated by the pulse length at -15 dB. One CP pulse length corresponds to 0.277 mm, while for REC, one pulse length corresponds to 0.169 mm. The bias and standard deviation of average scatterer diameter estimates for phantom S1 are shown in Fig. 5.

Simulations of phantom S2 consisted of obtaining average scatterer diameter estimates for the target lesion and the background region. The purpose of this simulation was to evaluate the quality of REC-QUS parametric images when 2 simulated tissues have a small difference in average scatterer diameter. Changes in standard deviation of average scatterer diameter estimates were obtained by varying the size of the axial gate with the simulations of phantom S2. For this study, the image quality metrics were the CNR and the histogram overlap, which were generated by assessing the lesion and background regions of the QUS

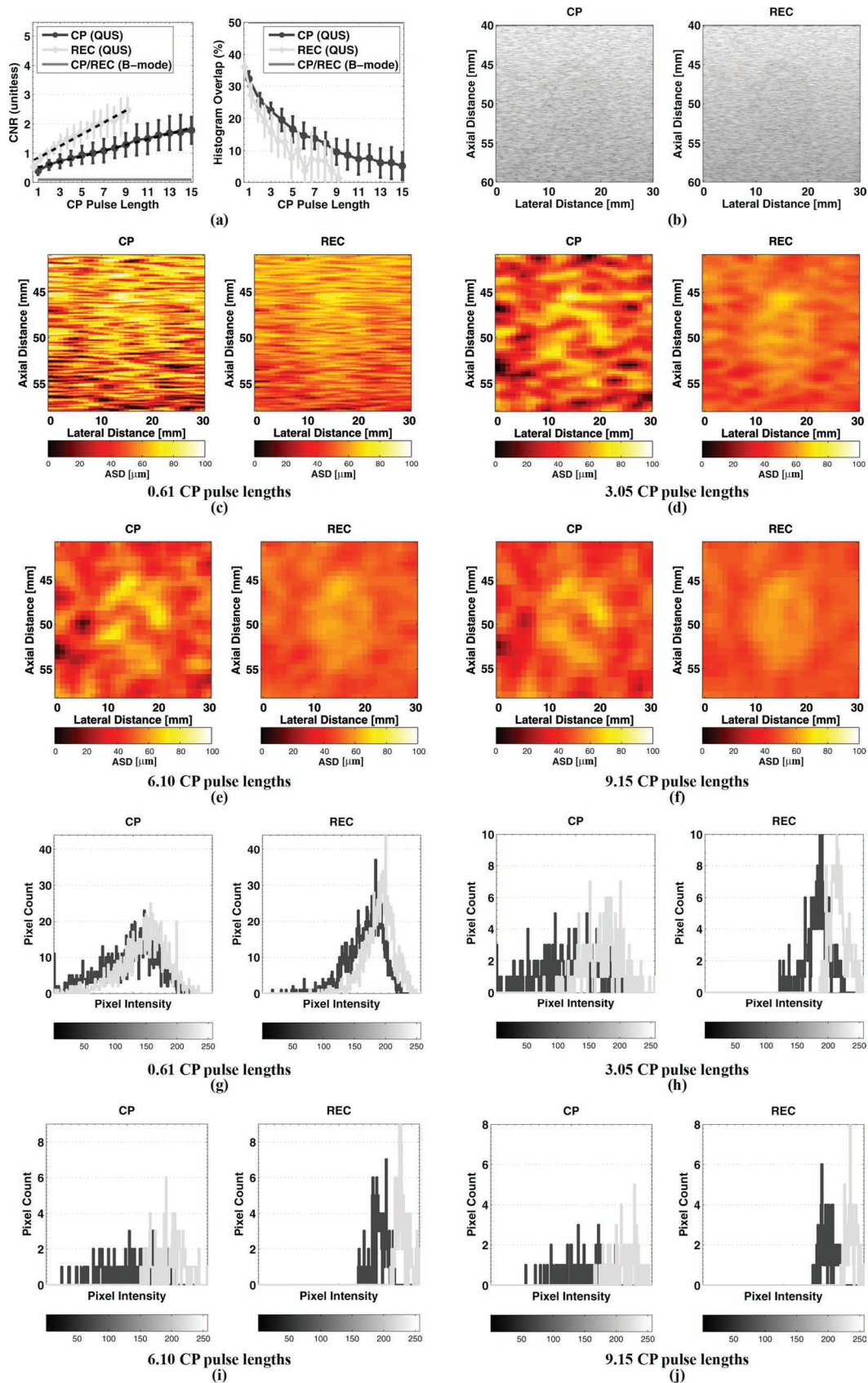


Fig. 6. (a) Contrast-to-noise ratio (CNR) and histogram overlap as a function of pulse length from 10 simulations of phantom S2. Each tick mark on the abscissa is normalized to a conventional pulsing (CP) pulse length of one, which corresponds to 0.277 mm. Therefore, one resolution enhancement compression (REC) pulse length, which is 0.169 mm, would correspond to 0.610 CP pulse length. (b) B-mode images of phantom S2 for CP and REC. (c)–(f) Parametric image of average scatterer diameter for phantom S2 for CP and REC for various axial lengths. Actual scatterer diameters for lesion and background region are 60 μm and 50 μm , respectively. (g)–(j) Histograms of average scatterer diameter distribution in the background and target regions for phantom S2 for various axial lengths (dark: background region, light: target region).

TABLE III. BIAS, HISTOGRAM OVERLAP, AND CNR \pm 1 STANDARD DEVIATION RESULTS FOR (10) PHANTOMS S2 AT DIFFERENT CP PULSE LENGTHS.¹

CP pulse lengths	Bias, μm				Histogram overlap, %		CNR, unitless	
	CP		REC		CP	REC	CP	REC
	Lesion	Background	Lesion	Background				
0.61	-0.10 ± 15.59	2.46 ± 18.30	7.69 ± 5.85	17.69 ± 6.60	36.70 ± 1.36	36.08 ± 1.99	0.31 ± 0.09	0.52 ± 0.07
3.05	-2.23 ± 9.69	-3.78 ± 12.97	-2.11 ± 3.35	7.88 ± 4.08	21.70 ± 3.29	15.72 ± 6.08	0.72 ± 0.23	1.36 ± 0.28
6.10	-2.07 ± 6.78	-3.85 ± 9.52	-5.44 ± 2.56	4.55 ± 3.17	13.75 ± 4.30	3.71 ± 4.66	1.02 ± 0.36	1.98 ± 0.45
9.15	-2.01 ± 5.41	-3.77 ± 6.89	-7.28 ± 2.08	2.71 ± 2.66	9.14 ± 4.28	1.27 ± 3.18	1.36 ± 0.46	2.47 ± 0.42

¹CNR = contrast-to-noise ratio; CP = conventional pulsing; REC = resolution enhancement compression.

TABLE IV. EXPERIMENTAL RESULTS OF OUT OF RANGE, AVERAGE SCATTERER DIAMETER (ASD), AND STANDARD DEVIATION OF ASD ESTIMATES FOR ALL DEPTHS (AXIAL DISTANCE) COMBINED FOR THE PHANTOMS DESCRIBED IN TABLE II.¹

Phantom	Out of range, %		ASD, μm		Standard deviation (ASD), μm	
	CP	REC	CP	REC	CP	REC
A	17.9	4.4	83.0	82.6	6.4	4.2
B	87.2	37.9	52.4	33.8	9.6	10.9
C	93.4	61.3	65.6	54.1	10.8	2.7
D	87.2	20.5	63.6	50.1	10.9	3.2

¹CP = conventional pulsing; REC = resolution enhancement compression.

parametric images. Evaluating CNR for the optimal axial length [26] of 15 REC pulse lengths, which is equivalent to 2.54 mm, the CNR was 1.28 ± 0.52 for CP and 2.47 ± 0.42 for REC. Comparisons of CNR as a function of CP pulse lengths for phantom S2 are shown in Fig. 6(a).

Histogram analysis further highlights the improvements obtained by using REC-QUS over conventional QUS. CNR allowed quantification of the improvement in contrast while histogram overlap was used to evaluate the overlap in intensity between QUS pixels in the lesion and background regions. In addition, histogram overlap allows quantification of the optimal gate length when examining the trade-off between axial resolution and contrast resolution. Note that analysis of the overlap regions does not contain ROIs that are near the perimeter of the lesion. Histogram overlap as a function of pulse length for phantom S2 is shown in Fig. 6(a).

Conventional B-mode images for phantom S2 are shown in Fig. 6(b). The CNR for the B-mode images of CP and REC shown in Fig. 6(b) was 0.14. The parametric images for the QUS estimates of average scatterer diameter for the following axial gate lengths: 0.61 CP pulse lengths (1 REC pulse length), 3.05 CP pulse lengths (5 REC pulse lengths), 6.10 CP pulse lengths (10 REC pulse lengths), and 9.15 CP pulse lengths (15 REC pulse lengths), are shown in in Figs. 6(c)–(f) while histograms corresponding to these are shown in Figs. 6(g)–(j). Bias, standard deviation, histogram overlap, and CNR for the parametric images shown in Figs. 6(c)–(f) and values for various CP pulse lengths are listed in Table III.

B. Experiments

B-mode images for CP and REC along with a parametric image overlay for all phantoms are shown in Figs.

7(a)–(d). Furthermore, the average scatterer diameter and standard deviation of average scatterer diameter estimates as a function of depth for all phantoms are shown in Figs. 7(e)–(h) while the results for out-of-range, average scatterer diameter, and standard deviation of average scatterer diameter estimates for all depths combined are shown in Table IV.

The average scatterer diameter results in Figs. 7(e)–(h) demonstrate that REC-QUS has a better ability to obtain improved estimates when compared with conventional QUS methods obtained with CP. Moreover, the standard deviation of average scatterer diameter estimates in Figs. 7(e)–(h) corroborate that improvements in standard deviation were obtained by increasing the usable bandwidth through REC. Furthermore, by using REC over CP, a decrease in the standard deviation of average scatterer diameter estimates of 34%, 75%, and 71% were obtained for phantoms A, C, and D, respectively.

IV. DISCUSSION AND CONCLUSIONS

A. Simulations

For phantom S1, the bias results in Fig. 5(a) demonstrate that REC-QUS obtained improved estimates when compared with conventional QUS methods using CP. Additionally, the standard deviation results in Fig. 5(b) provides evidence that the bandwidth enhancement generated by using REC resulted in significant improvements in estimation error. For ROIs of CP axial pulse lengths of one through 4, a mean decrease of 52% in standard deviation were obtained by using REC. Furthermore, by using REC over CP, an approximate 43% decrease in the standard deviation of average scatterer diameter estimates

was obtained for ROIs with axial pulse lengths greater than 4. More importantly, the standard deviation when evaluating at the optimal axial length [26] of 15 CP pulse lengths was found to be 7.09 for CP. For REC, the same standard deviation can be achieved with 1.33 CP pulse lengths. These results suggest that the same standard deviation that can be obtained with conventional QUS can be achieved by using REC-QUS but for a smaller axial pixel size for the parametric image. In fact, the axial pixel in the parametric image would be approximately less than twice the size of the axial pixel length in a conventional B-mode image.

For phantom S2, fitting the CNR data of Fig. 6(a) with a line in the least-squares sense provided a slope of 0.09 and an intercept of 0.41 for CP while a slope of 0.20 and an intercept of 0.64 was obtained for REC. These results suggest that a greater increase in contrast occurs using REC all the while improving QUS parametric image axial resolution as opposed to conventional QUS performed with CP. In fact, REC-QUS parametric images achieved an average of 38% increase in contrast when compared with the conventional QUS parametric images generated using CP. Furthermore, observation from Fig. 6(a) indicates that for REC-QUS, histogram overlap reaches approximately 0% for a gate length of 9.5 CP pulse lengths, while for conventional QUS, 0% is achieved at 17.3 CP pulse lengths. These results indicate that the optimal axial gate length was around 10 CP pulse lengths, where the parametric image using REC yielded optimal contrast. By using REC-QUS with a gate length of 10 CP pulse lengths as opposed to conventional QUS with a gate length of 17 CP pulse lengths, a gain of 70% in axial resolution in the parametric image was achieved.

Examination of the REC parametric images in Figs. 6(c)–(f) reveals that, by using REC-QUS, the lesion is more clearly observed in all cases when compared with conventional QUS methods for the same gate length. The contrast increased as the gate length increased. Furthermore, histogram analysis extends the notion of improved contrast and target detectability by showing the increased separation between the target and background as the gate length increased. These observations are supported by the improvements in contrast and reduction of histogram overlap as shown in Fig. 6(a). CNR results indicate that, with both REC-QUS and conventional QUS, an improvement in contrast can be achieved when compared with the conventional B-mode image shown in Fig. 6(b). In addition, the decrease in histogram overlap using REC-QUS led to improved detection and differentiation of the lesion from the background when compared with CP.

A further benefit of REC-QUS is observed by comparison of the bias and standard deviation for the background regions in REC and CP as shown in Table III. For example, for ROIs of 15 REC pulse lengths (9.15 CP pulse lengths) [26], the bias for CP was $-3.76 \mu\text{m}$ for the background and $-2.01 \mu\text{m}$ for the lesion, while the bias for REC was $2.71 \mu\text{m}$ for the background and $-7.28 \mu\text{m}$ for the lesion. Similarly, the standard deviation for ROIs of

15 REC pulse lengths (9.15 CP pulse lengths) for CP was $6.89 \mu\text{m}$ for the background and $5.41 \mu\text{m}$ for the lesion, while for REC, the standard deviation was $2.66 \mu\text{m}$ for the background and $2.08 \mu\text{m}$ for the lesion. These results suggest that, for conventional QUS, the standard deviation of average scatterer diameter deteriorates as the diameter of the scatterer decreases. Conversely, using REC, the performance of QUS is increased because it resulted in accurate estimates for a smaller scatterer diameter because of the large ka range obtained by increasing the usable bandwidth. This larger ka range suggests that, by using REC-QUS, scatterers with different diameters could be quantified by using the same transducer as opposed to conventional QUS sources where multiple sources are needed.

Recall that the difference in scatterer diameter between the lesion and the background is $10 \mu\text{m}$. The trade-off between axial length and standard deviation will be evaluated for this small difference in scatterer diameter. Fig. 6(c) has poor contrast when compared with Fig. 6(f); however, the axial pixel length is the same as the B-mode image in Fig. 6(b), which would allow smaller targets to be detected. Conversely, Fig. 6(f) has great contrast when compared with Fig. 6(c); however, axial pixel length is 15 times the axial pixel length of the B-mode image in Fig. 6(b). As a result, this axial pixel length will provide a smooth high contrast image but at the expense of potentially not detecting smaller targets. Naturally, targets could be easily detected if the difference in scatterer diameter would be larger. In summary, REC-QUS can be used to extend the trade-off between axial length and contrast to improve target detectability.

B. Experiments

The average scatterer diameter results in Figs. 7(e)–(h) demonstrate that REC-QUS has a better ability to obtain improved estimates when compared with conventional QUS methods obtained with CP. Moreover, the standard deviation of average scatterer diameter estimates in Figs. 7(e)–(h) corroborate that improvements in standard deviation were obtained by increasing the usable bandwidth through REC. Furthermore, by using REC over CP, a decrease in the standard deviation of average scatterer diameter estimates of 34%, 75%, and 71% were obtained for phantoms A, C, and D, respectively.

The standard deviation from combining all QUS average scatterer diameter estimates for phantom B as shown in Table IV was 9.6 for CP and 10.9 for REC. At first glance, these results suggest that conventional QUS is preferable over REC-QUS. Evaluating the results in Fig. 7(f), the standard deviation of REC-QUS was always lower than conventional QUS by using CP at any particular depth. However, analysis using Fig. 7(b) along with Fig. 7(f) helps explain why the standard deviation of QUS average scatterer diameter estimates using all depths combined is larger for REC when compared with CP. In REC-QUS, the average scatterer diameter decreases as the depth in-

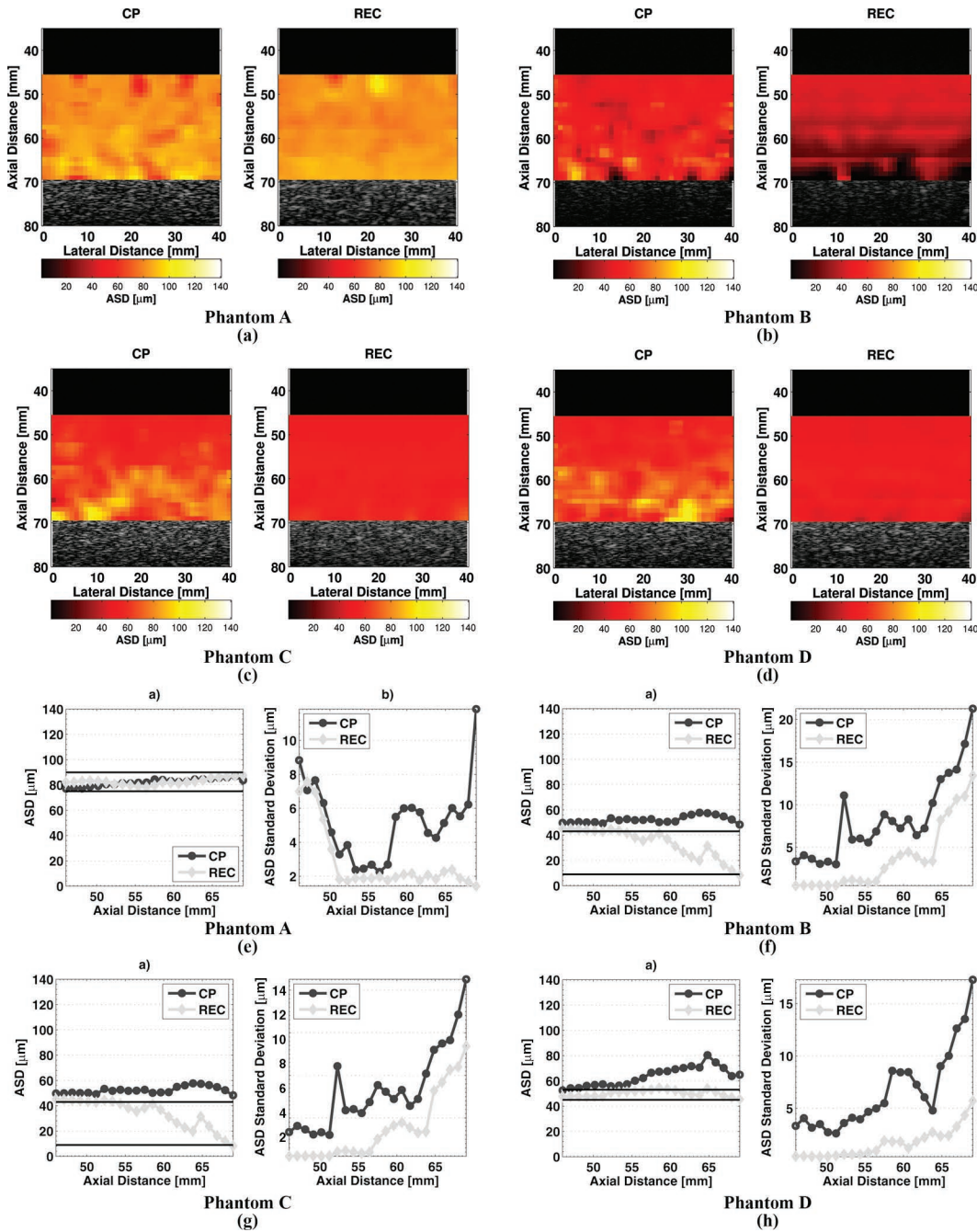


Fig. 7. (a)–(d) B-mode images for conventional pulsing (CP) and resolution enhancement compression (REC) with a parametric image overlay of average scatterer diameter. (e)–(h) Average scatterer diameter and standard deviation of average scatterer diameter estimates as a function of axial distance. The range of scatterers is indicated by solid lines across as a function of depth.

creases, causing a large standard deviation when calculating the standard deviation from all depths combined. As a consequence, conventional QUS had a better overall standard deviation but a poor predictive ability because the majority of estimated values were out of the range of scatterers in the phantom.

Overall, as the penetration depth increased, the improvements in the standard deviation of average scatterer diameter estimates using REC increased. This improvement was due to the increase in eSNR by using coded excitation and the increase in the bandwidth. REC-QUS

resulted in more accurate average scatterer diameter estimates because REC-QUS obtained a larger percentage of estimates that were within the true range of scatterer diameters.

REC-QUS extended the results by Kanzler and Oelze [27]. In [27], improved estimation bias versus penetration depth was obtained because of the increase in eSNR by using coded excitation. REC can achieve similar results because it produces an increase in eSNR by exciting the source with a preenhanced chirp. In addition, the extension to the work comes from using the preenhanced chirp,

which increased the usable bandwidth by a factor of 2. Therefore, the results were extended by combining REC with QUS techniques because the larger usable bandwidth resulted in a reduction in the standard deviation of average scatterer diameter estimates. Smaller standard deviations aid in the classification of tumors and tissue typing.

Previous studies have indicated that simple QUS techniques can differentiate between different kinds of tumors in animal models of cancer [21], [22]. Specifically, a study by Oelze and Zachary [21], [22] evaluated conventional QUS techniques *in vivo* on mice with transplanted 4T1 mammary carcinomas and EHS sarcomas. The objective of the study was to classify between the 2 types of tumors; however, estimates of average scatterer diameter and average acoustic concentration contained a significant amount of overlap between the estimates. Furthermore, in that study, statistical differences were only observed when the bandwidth was limited to certain regions of the power spectra. By having more available bandwidth for estimates, it is more likely that, with REC-QUS, one can choose regions that will yield estimates that produce statistically significant differences. Therefore, in a preclinical and clinical setting, REC-QUS has a greater potential to improve the differentiation between these different types of tumors markedly because of the reduced estimate variance, lesion-to-background contrast, larger *ka* range, and smaller axial pixel length. A significant advantage that REC-QUS has over conventional techniques is that the analysis bandwidth can be partitioned to section the power spectrum into different scales because different scatterers are sensitive to certain frequencies. In other words, REC-QUS has the potential to assess tissues using multiple scales with one source as opposed to conventional QUS technique where multiple sources with different center frequencies may be needed.

A potential limitation of REC-QUS is the fact that sources with larger bandwidth tend to have a large center frequency shift due to the frequency-dependent attenuation. Besides the center frequency shift, a decrease in the bandwidth is encountered that would effectively reduce the variance improvements obtained with REC-QUS. However, it should be noted that Phantom C and Phantom D contained scatterers in the range of 45 to 53 μm diameters but different attenuation coefficients 0.5 and 0.8 dB $\text{MHz}^{-1}\text{cm}^{-1}$, respectively. Therefore, because of the higher attenuation coefficient in Phantom D, the standard deviation of the average scatterer diameter estimates when using REC-QUS increased by 18%. As a comparison, with conventional QUS, a 1% increase in the standard deviation of the average scatterer was observed. Nonetheless, a 70% decrease in the standard deviation of average scatterer diameter was obtained when using REC-QUS over conventional QUS.

Another potential limitation of REC-QUS technique is the possibility of transducer heating, which may pose a patient safety problem. When transmitting a preenhanced chirp into a transducer, an increase in energy at the inefficient frequency bands of the transducer exists, which

could lead to the conversion of electrical energy into heat. Future experiments will examine the trade-offs between exciting sources with preenhanced chirps and additional heating of the transducer. Further studies will examine the REC-QUS technique for improvements in average acoustic concentration because the average acoustic concentration is dependent on initial estimate of average scatterer diameter.

ACKNOWLEDGMENT

The authors would like to thank S. G. Kanzler, R. J. Lavarello, and Dr. W. D. O'Brien, Jr. for the useful discussions.

REFERENCES

- [1] F. L. Lizzi, M. Greenebaum, E. J. Feleppa, M. Elbaum, and D. J. Coleman, "Theoretical framework for spectrum analysis in ultrasonic characterization," *J. Acoust. Soc. Am.*, vol. 73, pp. 1366–1373, Jan. 1983.
- [2] D. J. Coleman and F. L. Lizzi, "Computerized ultrasonic tissue characterization of ocular tumors," *Am. J. Ophthalmol.*, vol. 96, pp. 165–175, Aug. 1983.
- [3] E. J. Feleppa, F. L. Lizzi, D. J. Coleman, and M. M. Yaremko, "Diagnostic spectrum analysis in ophthalmology: A physical perspective," *Ultrasound Med. Biol.*, vol. 12, pp. 623–631, Aug. 1986.
- [4] F. L. Lizzi, M. Ostromogilsky, E. J. Feleppa, M. C. Rorke, and M. M. Yaremko, "Relationship of ultrasonic spectral parameters to features of tissue microstructures," *IEEE Trans. Ultrason. Ferroelectr. Freq. Control*, vol. 34, no. 3, pp. 319–329, 1987.
- [5] R. H. Silverman, D. J. Coleman, F. L. Lizzi, J. H. Torpey, J. Driller, T. Iwamoto, S. E. P. Burgess, and A. Rosado, "Ultrasonic tissue characterization and histopathology in tumor xenografts following ultrasonically induced hyperthermia," *Ultrasound Med. Biol.*, vol. 12, pp. 639–645, Aug. 1986.
- [6] D. J. Coleman, R. H. Silverman, M. J. Rondeau, F. L. Lizzi, J. W. McLean, and F. A. Jakobiec, "Correlations of acoustic tissue typing of malignant-melanoma and histopathologic features as a predictor of death," *Am. J. Ophthalmol.*, vol. 110, pp. 380–388, Oct. 1990.
- [7] D. J. Coleman, R. H. Silverman, M. J. Rondeau, J. A. Coleman, D. Rosberger, R. M. Ellsworth, and F. L. Lizzi, "Ultrasonic tissue characterization of uveal melanoma and prediction of patient survival after enucleation and brachytherapy," *Am. J. Ophthalmol.*, vol. 112, pp. 682–688, Dec. 1991.
- [8] R. L. Romijn, J. M. Thijssen, B. J. Oosterveld, and A. M. Verbeek, "Ultrasonic differentiation of intraocular melanomas: Parameters and estimation methods," *Ultrasound Imaging*, vol. 13, pp. 27–55, Jan. 1991.
- [9] F. L. Lizzi, M. Astor, T. Liu, C. Deng, D. J. Coleman, and R. H. Silverman, "Ultrasonic spectrum analysis for tissue assays and therapy evaluation," *Int. J. Imaging Syst. Technol.*, vol. 8, no. 8, pp. 3–10, 1997.
- [10] R. C. Waag, P. P. K. Lee, H. W. Persson, E. A. Schenk, and R. Gramiak, "Frequency-dependent angle scattering of ultrasound by liver," *J. Acoust. Soc. Am.*, vol. 72, pp. 343–352, Jan. 1982.
- [11] F. L. Lizzi, D. L. King, M. C. Rorke, M. Ostromogilsky, M. M. Yaremko, E. J. Feleppa, and P. Wai, "Comparison of theoretical scattering results and ultrasonic data from clinical liver examinations," *Ultrasound Med. Biol.*, vol. 14, no. 5, pp. 377–385, 1988.
- [12] M. F. Insana, J. G. Wood, and T. J. Hall, "Identifying acoustic scattering sources in normal renal parenchyma *in vitro* by varying arterial and ureteral pressures," *Ultrasound Med. Biol.*, vol. 18, no. 6–7, pp. 587–599, 1992.
- [13] J. A. Zagzebski, Z. Flu, and L. X. Xiao, "Quantitative ultrasound imaging: *In vivo* results in normal liver," *Ultrasound Imaging*, vol. 15, pp. 335–351, Oct. 1993.
- [14] E. J. Feleppa, A. Kalisz, J. B. Sokil-Melgar, F. L. Lizzi, L. Tian, A. L. Rosado, M. C. Shao, W. R. Fair, W. Yu, M. S. Cookson, V. E.

- Reuter, and W. D. W. Heston, "Typing of prostate tissue by ultrasonic spectrum analysis," *IEEE Trans. Ultrason. Ferroelectr. Freq. Control*, vol. 43, pp. 609–619, Jul. 1996.
- [15] E. J. Feleppa, T. Liu, A. Kalisz, M. C. Shao, N. Fleshner, and V. Reuter, "Ultrasonic spectral-parameter imaging of the prostate," *Int. J. Imaging Syst. Technol.*, vol. 8, no. 1, pp. 11–25, 1997.
- [16] F. T. D'Astous and F. S. Foster, "Frequency dependence of ultrasound attenuation and backscatter in breast tissue," *Ultrasound Med. Biol.*, vol. 12, pp. 795–808, Oct. 1986.
- [17] R. M. Golub, R. E. Parsons, B. Sigel, E. J. Feleppa, J. Justin, H. A. Zaren, M. Rorke, J. Sokil-Melgar, and H. Kimitsuki, "Differentiation of breast tumors by ultrasonic tissue characterization," *J. Ultrasound Med.*, vol. 12, pp. 601–608, Oct. 1993.
- [18] K. A. Topp, J. F. Zachary, and W. D. O'Brien Jr., "Quantifying B-mode images of *in vivo* rat mammary tumor with frequency dependence of backscatter," *J. Ultrasound Med.*, vol. 20, pp. 605–612, Jun. 2001.
- [19] M. L. Oelze, J. F. Zachary, and W. D. O'Brien Jr., "Parametric imaging of rat mammary tumors *in vivo* for purposes of tissue characterization," *J. Ultrasound Med.*, vol. 21, pp. 1201–1210, Nov. 2002.
- [20] M. L. Oelze, J. F. Zachary, and W. D. O'Brien Jr., "Characterization of tissue microstructure using ultrasonic backscatter: Theory and technique optimization using a Gaussian form factor," *J. Acoust. Soc. Am.*, vol. 112, pp. 1202–1211, Sep. 2002.
- [21] M. L. Oelze, J. F. Zachary, and W. D. O'Brien Jr., "Differentiation and characterization of mammary fibroadenomas and 4T1 carcinomas using ultrasound parametric imaging," *IEEE Trans. Med. Imaging*, vol. 23, pp. 764–771, Jun. 2004.
- [22] M. L. Oelze and J. F. Zachary, "Examination of cancer in mouse models using high frequency quantitative ultrasound," *Ultrasound Med. Biol.*, vol. 32, pp. 1639–1648, Nov. 2006.
- [23] S.L. Bridal, P. Fornès, P. Bruneval, and G. Berger, "Parametric (integrated backscatter and attenuation) images constructed using backscattered radio frequency signals (25–56 MHz) from human aortae *in vitro*," *Ultrasound Med. Biol.*, vol. 23, no. 2, pp. 215–229, 1997.
- [24] A. Nair, B. D. Kuban, N. Obuchowski, and D. G. Vince, "Assessing spectral algorithms to predict atherosclerotic plaque composition with normalized and raw intravascular ultrasound data," *Ultrasound Med. Biol.*, vol. 27, pp. 1319–1331, Oct. 2001.
- [25] M. F. Insana, "Modeling acoustic backscatter from kidney microstructure using an anisotropic correlation function," *J. Acoust. Soc. Am.*, vol. 97, pp. 649–655, Jan. 1995.
- [26] M. L. Oelze and W. D. O'Brien Jr., "Defining optimal axial and lateral resolution for estimating scatterer properties from volumes using ultrasound backscatterer," *J. Acoust. Soc. Am.*, vol. 115, pp. 3226–3234, Jun. 2004.
- [27] S. G. Kanzler and M. L. Oelze, "Improved scatterer size estimation using backscatter coefficient measurements with coded excitation and pulse compression," *J. Acoust. Soc. Am.*, vol. 123, pp. 4599–4607, Jun. 2008.
- [28] M. L. Oelze, "Bandwidth and resolution enhancement through pulse compression," *IEEE Trans. Ultrason. Ferroelectr. Freq. Control*, vol. 54, pp. 768–781, Apr. 2007.
- [29] P. Chaturvedi and M. F. Insana, "Error bounds on ultrasonic scatterer size estimates," *J. Acoust. Soc. Am.*, vol. 100, pp. 392–399, Jul. 1996.
- [30] J. K. Tsou, J. Liu, and M. F. Insana, "Modeling and phantom studies of ultrasonic wall shear rate measurements using coded excitation," *IEEE Trans. Ultrason. Ferroelectr. Freq. Control*, vol. 53, pp. 724–734, Apr. 2006.
- [31] M. F. Insana, R. F. Wagner, D. G. Brown, and T. J. Hall, "Describing small-scale structure in random media using pulse-echo ultrasound," *J. Acoust. Soc. Am.*, vol. 87, pp. 179–192, Jan. 1990.
- [32] M. F. Insana and T. J. Hall, "Parametric ultrasound imaging from backscatter coefficient measurements: Image formation and interpretation," *Ultrason. Imaging*, vol. 12, pp. 245–267, Oct. 1990.
- [33] J. A. Jensen, "A model for the propagation and scattering of ultrasound tissue," *J. Acoust. Soc. Am.*, vol. 89, pp. 182–190, Jan. 1991.
- [34] D. Nicholas, "Evaluation of backscattering coefficients for excised human tissues: Results, interpretation, and associated measurements," *Ultrasound Med. Biol.*, vol. 8, no. 1, pp. 17–28, 1982.
- [35] D. K. Nassiri and C. R. Hill, "The use of angular scattering measurements to estimate structural parameters of human and animal tissues," *J. Acoust. Soc. Am.*, vol. 79, pp. 2048–2054, Jan. 1986.
- [36] M. F. Insana and T. J. Hall, "Parametric ultrasound imaging from backscatter coefficient measurements: Image formation and interpretation," *Ultrason. Imaging*, vol. 12, pp. 245–267, Oct. 1990.
- [37] K. Raum and W. D. O'Brien Jr., "Pulse-echo field distribution measurement technique for high-frequency ultrasound sources," *IEEE Trans. Ultrason. Ferroelectr. Freq. Control*, vol. 44, pp. 810–815, Jul. 1997.
- [38] K. A. Wear, T. A. Stiles, G. R. Frank, E. L. Madsen, F. Cheng, E. J. Feleppa, C. S. Hall, B. S. Kim, P. Lee, W. D. O'Brien Jr., M. L. Oelze, B. I. Raju, K. K. Shung, T. A. Wilson, and J. R. Yuan, "Interlaboratory comparison of ultrasonic backscatter coefficient measurements from 2 to 9 MHz," *J. Ultrasound Med.*, vol. 24, pp. 1235–1250, Sep. 2005.
- [39] E. L. Madsen, F. Dong, G. R. Frank, B. S. Garra, K. A. Wear, T. A. Wilson, J. A. Zagzebski, H. L. Miller, K. K. Shung, S. H. Wang, E. J. Feleppa, T. Liu, W. D. O'Brien Jr., K. A. Topp, N. T. Sanghvi, A. V. Zaitsev, T. J. Hall, J. B. Fowlkes, O. D. Kripfgans, and J. G. Miller, "Interlaboratory comparison of ultrasonic backscatter, attenuation, and speed measurements," *J. Ultrasound Med.*, vol. 18, pp. 615–631, Sep. 1999.
- [40] J. J. Faran, "Sound scattering by solid cylinders and spheres," *J. Acoust. Soc. Am.*, vol. 23, pp. 405–418, 1951.
- [41] R. Hickling, "Analysis of echoes from a solid elastic sphere in water," *J. Acoust. Soc. Am.*, vol. 34, no. 10, pp. 1582–1592, 1962.
- [42] M. S. Patterson and F. S. Foster, "The improvement and quantitative assessment of B-mode images produced by an annular array/cone hybrid," *Ultrason. Imaging*, vol. 5, no. 3, pp. 195–213, 1983.



Jose R. Sanchez was born in Houston, TX, in 1977. He earned his B.S. and M.S. degrees in electrical engineering in 2000 and 2002 from Bradley University, Peoria, IL. As of 2005, Mr. Sanchez has been pursuing a doctoral degree in electrical engineering at the University of Illinois at Urbana-Champaign.

In the fall of 2009, Mr. Sanchez will be an assistant professor at Bradley University in the Electrical and Computer Engineering Department. His research interests include embedded signal processing, ultrasonic imaging, application of coded excitation techniques in ultrasound, and quantitative ultrasound.

Mr. Sanchez is a student member of the IEEE, the IEEE UFFC Society, and a member of the Acoustical Society of America.

Darren Pocci was born in Downers Grove, IL, in 1986. He earned his B.S. degree in electrical engineering in 2008 from the University of Illinois at Urbana-Champaign. As of the fall of 2008, he is pursuing his M.S. degree in electrical engineering also at the University of Illinois with a planned graduation in 2010. His research interests include multi-dimensional signal processing and cardiac applications in magnetic resonance imaging. Mr. Pocci is student member of the IEEE.



Michael L. Oelze was born in Hamilton, New Zealand, in 1971. He earned his B.S. degree in physics and mathematics in 1994 from Harding University, Searcy, AR; his M.S. degree in physics in 1996 from the University of Louisiana at Lafayette, Lafayette, LA; and his Ph.D. degree in physics in 2000 from the University of Mississippi, Oxford, MS.

Dr. Oelze was a post-doctoral fellow at the University of Illinois at Urbana-Champaign from 2000 to 2004 conducting research in ultrasound.

His research interests include the acoustic interaction with soil, ultrasound tissue characterization, quantitative ultrasound, ultrasound bio-effects, ultrasound tomography techniques, and application of coded excitation to ultrasound imaging. Currently, Dr. Oelze is an assistant professor at the University of Illinois at Urbana-Champaign.

Dr. Oelze is a member of the IEEE, the IEEE UFFC Society, the American Institute for Ultrasound in Medicine, and the Acoustical Society of America.